Inorganic Chemistry

Article

pubs.acs.org/IC

New Layered Compounds with Honeycomb Ordering: $Li_3Ni_2BiO_6$, $Li_3NiM'BiO_6$ (M′ = Mg, Cu, Zn), and the Delafossite $Ag_3Ni_2BiO_6$

Romain Berthelot,[†] Whitney Schmidt,[†] Sean Muir,[†] James Eilertsen,[†] Laetitia Etienne,[‡] A. W. Sleight,[†] and M. A. Subramanian*,[†]

[†]Department of Chemistry, Oregon State University, Corvallis, Oregon 97331, United States

[‡]CNRS, Université de Bordeaux, ICMCB, 87 avenue du Dr. A. Schweitzer, 33608 F-Pessac, France

Supporting Information

ABSTRACT: The new layered compound $Li_3Ni_2BiO_6$ has been prepared by a solid-state reaction. It crystallizes in the monoclinic *C*2/*m* space group; its lamellar structure is characterized by a honeycomb ordering between Ni^{2+} and Bi^{5+} within the slabs, while Li^+ ions occupy octahedral sites in the interslab space. Stacking defects weakly alter the XRD pattern. By substitution of half of the nickel ions, the new phases $Li_3NiM'BiO_6$ (M′ = Mg, Cu, Zn) isostructural with $Li_3Ni_2BiO_6$ have been synthesized under similar conditions. All these compounds demonstrate paramagnetic behavior at high temperature, and $Li_3Ni_2BiO_6$ exhibits an antiferromagnetic ordering at 5.5 K. By topotactic molten salt ionic exchange, the new delafossite compound $Ag_3Ni_2BiO_6$ has been also obtained and characterized.

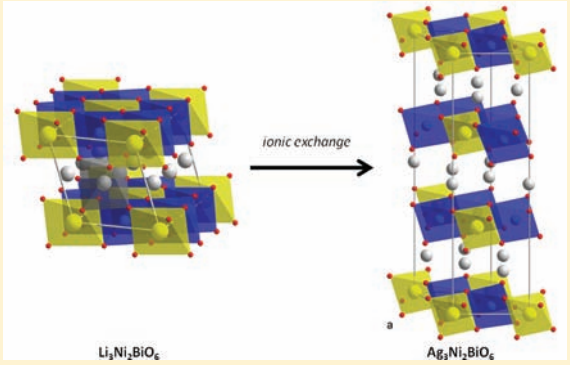

1. INTRODUCTION

The variation in details of the structures of layered ternary oxides AMO_2, such as the stacking sequence of local symmetries, plays a key role in their various and remarkable properties. Among the wide range of available AMO_2 compositions, some of them have attracted research interest because of their outstanding properties and applications, such as a positive electrode material in Li ion batteries for $LiCoO_2$[1] or as a transparent conducting oxide for $CuAlO_2$.[2]

The layered structure of these AMO_2 compounds is usually described as a stacking of edge-shared MO_6 octahedra layers forming MO_2 slabs, between which A^+ cations are intercalated. The M element is a trivalent cation, while A is typically an alkaline or noble metal (Ag, Cu, Pd, or Pt[3]). Depending on the nature of this cation, its content (A_xMO_2, with $x \leq 1$), and the synthetic procedure, different intercalation sites are observed for A in the interslab space: octahedral, trigonal prismatic, tetrahedral, or linear for the delafossites (O−A−O dumbbell configuration). A nomenclature has been introduced to clarify all these stackings: it consists of a letter standing for the intercalation site symmetry (O, P, T, and D) and a numeral to indicate the number of slabs in the hexagonal unit cell.[4,5]

The AMO_2 structure can be modified to expand the chemistry and obtain interesting new compositions by partially substituting the M site with a different X element. M and X can adopt either the same or a different oxidation state. In the latter case, the M and X cations can be either disordered or ordered in the slab plane.

Recently, many studies have been reported on $A_3M^{2+}{}_2X^{5+}O_6$ (i.e., $AM_{2/3}X_{1/3}O_2$) and $A_2M^{2+}{}_2X^{6+}O_6$ (i.e., $A_{2/3}M_{2/3}X_{1/3}O_2$) phases exhibiting an M/X ordering in the slab. In this particular ordering, each XO_6 octahedron is surrounded in the slab by six MO_6 octahedra. Therefore, the M cation arrangement follows a honeycomb model (Figure 1). Most of $A_3M_2XO_6$ phases contain Sb^{5+} as the X cation: e.g. $Li_3M_2SbO_6$ (M = Ni, Cu, Zn[6−9]) and $Na_3M_2SbO_6$ (M = Mg, Co, Ni, Cu, Zn[10−12]). Here the structure adopts an O3 stacking: Li^+ or Na^+ cations occupy an octahedral site sharing edges with surrounding MO_6 or SbO_6 octahedra (Figure 1). Note that many other layered compounds adopt the same honeycomb structure with different oxidation states for both M and X cations: e.g. the phases A_2MO_3 (i.e., $AM^{4+}{}_{2/3}A^+{}_{1/3}O_2$, A = Li, Na)[13−16] and A_5XO_6 (i.e., $AA^+{}_{2/3}X^{7+}{}_{1/3}O_2$, A = Li, Na).[17,18]

The honeycomb ordering involves a change in the unit cell based on the $\sqrt{3}a_0 \times \sqrt{3}a_0$ in-plane superstructure, a_0 being the in-plane lattice parameter in the hexagonal description of the AMO_2 cell. To emphasize this honeycomb ordering, Politaev et al. proposed to complete the aforementioned nomenclature and to designate this stacking O3*S* (with *S* standing for superstructure).[12]

All the reported $A_2M_2XO_6$ phases contain Te^{6+} as the X cation and Na^+ as the interslab filler. The M cation can be respectively Mg, Co, Ni, Cu, and Zn.[10,19,20] Except for $Na_2Cu_2TeO_6$, which adopts the O3*S* stacking, the layer stacking is P2 for all the others phases (or P2*S*): Na^+ cations occupy trigonal-prismatic NaO_6 sites sharing either faces or edges with surrounding MO_6 or TeO_6 octahedra (structure not shown here).

Received: February 16, 2012
Published: April 19, 2012

   dx.doi.org/10.1021/ic300351t | *Inorg. Chem.* 2012, 51, 5377−5385

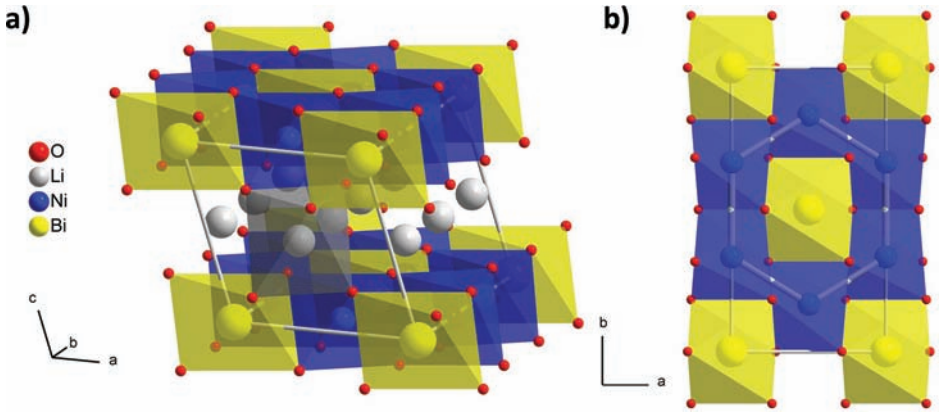

Figure 1. (a) Representation of the $A_3M_2XO_6$ structure in the case of $Li_3Ni_2BiO_6$ in perspective view, evidencing the layered organization of $Ni_{2/3}Bi_{1/3}O_2$ slabs (blue and yellow edge-shared octahedra) and LiO_2 interslab (in gray, only one octahedron is drawn for clarity). (b) Representation along the monoclinic *c* axis highlighting the honeycomb-type Ni^{2+}/Bi^{5+} ordering within the slab.

The honeycomb ordering can be also found in some delafossites. Nagarajan et al. prepared $Cu_3M_2SbO_6$ (M = Mn, Mg, Zn) directly from the component oxides,[21] and the synthesis of Cu_5SbO_6 (i.e., $Cu_3Cu_2SbO_6$) was also recently reported.[22] Topotactic molten salt ionic exchange has been used to prepare silver-based delafossite analogues, such as $Ag_3Co_2SbO_6$[12] and $Ag_3M_2LiO_6$ (M = Ti, Sn, Rh, Ir).[23,24]

In their report on the honeycomb-ordered layered phase $Li_3Zn_2SbO_6$, Greaves et al. briefly mentioned the synthesis of an isostructural $Li_3Zn_2BiO_6$ phase, but they did not study it in detail.[6] It is to our knowledge the only Bi^{5+}-based compound in the $A_3M_2XO_6$ family. Following this work, we tried to complete the $Li_3M_2BiO_6$ series with M standing for all the aforementioned bivalent cations. In this paper, we report the first synthesis and the first characterizations of a new honeycomb-ordered layered $Li_3Ni_2BiO_6$ phase and substituted $Li_3NiM'BiO_6$ (M′ = Mg, Cu, Zn) analogues, as well as the new delafossite $Ag_3Ni_2BiO_6$, prepared by topotactic ionic exchange following a molten salt method. The electrochemical properties of $Li_3Ni_2BiO_6$ as the positive electrode materials of a Li ion battery are also presented.

2. EXPERIMENTAL SECTION

Polycrystalline samples were prepared by conventional solid-state reactions. Lithium carbonate (Li_2CO_3; Aldrich 99.6%), nickel oxide (NiO, Alfa Aesar 99.998%), and bismuth oxide (Bi_2O_3, Aldrich 99.99%) were thoroughly ground together in an agate mortar in stoichiometric proportions to obtain $Li_3Ni_2BiO_6$. In order to avoid any moisture contamination, lithium carbonate was dried overnight at ∼120 °C before weighing. The pale green nominal mixture was then pelletized and heated in a gold crucible in air or O_2 flow over 12−48 h (with intermediate grinding) in the temperature range 550−900 °C with a heating rate of +2 °C min^{-1}. At the end of the thermal treatment, the furnace was switched off and the samples remained in the furnace during the cooldown. Other compositions $Li_3NiM'BiO_6$ (with M′ = Mg, Cu, Zn) were prepared under the same thermal conditions by mixing magnesium oxide (MgO, Alfa Aesar 99.95%), copper oxide (CuO, Aldrich 99.95%), or zinc oxide (ZnO, Aldrich 99.9%) with the previous precursors in the stoichiometric proportions.

Ion exchange was performed by mixing the obtained product $Li_3Ni_2BiO_6$ with silver nitrate ($AgNO_3$, Alfa Aesar 99.9%) in a large excess (ratio $Ag^+/Li^+ \approx 5$). The mixture was placed in a porcelain crucible and heated overnight at 230−250 °C to ensure the melting of the nitrate. The resulting product was then intensely washed with hot distilled water with magnetic stirring to dissolve the remaining nitrates and then filtered and finally dried overnight in an oven at ∼50 °C.

The powder of each sample was first characterized by X-ray diffraction (XRD) using a Rigaku Miniflex II diffractometer with Cu Kα radiation selected by a graphite monochromator on the diffracted beam. Powder samples were loaded onto an oriented Si single crystal "zero background" sample holder (MTI Corp.) to maximize the possibility of detecting minor impurity phases. Measurements were collected from 5 to 120° 2θ (step of 0.02°) with a 2 s fixed time.

Chemical compositions as well as ionic exchange quantifications were determined by inductively coupled plasma absorption electron spectroscopy (ICP-AES) on a Varian 720 ES instrument. Powder samples (∼10 mg) were dissolved in a high-quality hydrochloric acid solution heated at 70 °C with constant stirring.

Scanning electron microscopy (SEM) analysis was performed with a FEI Quanta 600F microscope. Sample powders were spread onto a conductive carbon tape that was metalized with Au/Pd sputtering to avoid charging.

Delafossite thermal stability was determined by thermogravimetric analysis (TGA) using a Mettler Toledo TGA 850 instrument. Sample powders were heated to 800 °C in air for 2 h (heating and cooling set to respectively +5 and −5° min^{-1}), and XRD was performed on the final product to identify the remaining phases.

Magnetism measurements were carried out on a Quantum Design physical properties measurement system (PPMS) in the temperature range 5−300 K under a magnetic field of 1 T and zero-field cooled conditions. A second run was slowly performed from 3 to 20 K to clarify the very low temperature behavior.

Electrochemical studies were carried out with Li_{metal}/liquid electrolyte/$Li_3Ni_2BiO_6$ cells. Merck Chemicals LP30 was used as the liquid electrolyte (1 M $LiPF_6$ in ethylene carbonate/diethyl carbonate 1/1). The positive electrode consisted of a mixture of 88 wt % of the active material (i.e., $Li_3Ni_2BiO_6$), 2 wt % of polytetrafluoroethylene, and 10 wt % of graphite/carbon black mix (1/1) to improve the general conductivity. Lithium sheet was used as the negative electrode. The cells were assembled in an argon-filled glovebox. The batteries were relaxed one night before operating in galvanostatic mode at a C/20 rate (i.e., 20 h is required to remove 3 electrons/mol of $Li_3Ni_2BiO_6$). After cycling, the positive electrode was washed with dimethyl carbonate in order to perform XRD.

3. RESULTS AND DISCUSSION

a. Characterization of $Li_3Ni_2BiO_6$. Greaves et al. reported the synthesis of $Li_3Zn_2BiO_6$ with a heat treatment at 600 °C under oxygen flow.[6] By following these conditions with the nominal $Li_3Ni_2BiO_6$ composition, we obtained a dark green pellet and noticed a mass loss of approximately 10.5%. This value matches with the theoretical mass loss according to eq 1.

dx.doi.org/10.1021/ic300351t | Inorg. Chem. 2012, 51, 5377−5385

$$^{3}/_{2}Li_2CO_3 + 2NiO + {}^{1}/_{2}Bi_2O_3 + {}^{5}/_{2}O_2 \rightarrow Li_3Ni_2BiO_6 + 3CO_2 \quad (1)$$

Figure 2 shows the XRD pattern of the final product. All the diffraction peaks can be indexed by a profile matching with the monoclinic space group $C2/m$ and cell parameters a = 5.2581(4) Å, b = 9.116(1) Å, c = 5.1969(8) Å, and β = 109.33(1)°. The XRD pattern is very similar to that obtained for $Li_3Ni_2SbO_6$[9] and $Na_3Ni_2SbO_6$.[12] According to these observations, the formation of a $Li_3Ni_2BiO_6$ phase adopting the same layered structure with a Ni^{2+}/Bi^{5+} honeycomb ordering (Figure 1) can be assumed. In addition, ICP-AES analysis shows the cationic ratios Ni/Bi ≈ 2 and Li/(Ni + Bi) ≈ 1, agreeing with the expected composition $Li_3Ni_2BiO_6$.

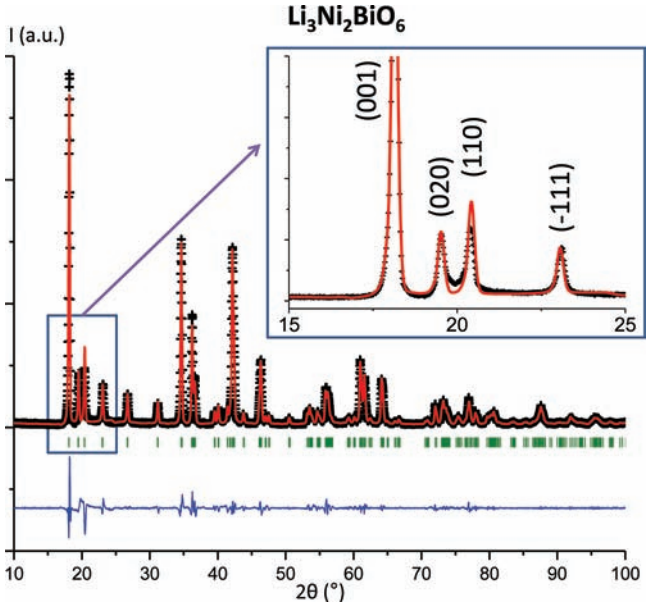

Figure 2. Experimental XRD pattern of $Li_3Ni_2BiO_6$ (observed, calculated (profile matching), and difference profiles respectively as black crosses and red and blue lines; Bragg positions as green vertical lines). The inset focuses on the 15−25° 2θ region to highlight the peak broadening due to stacking faults which avoid a good profile fitting.

However, the profile of the XRD pattern could not be refined satisfactorily using a pseudo-Voigt function, since some peaks exhibit significant asymmetric line broadening, especially in the 15−25° 2θ region (inset of Figure 2). This phenomenon was already noticed for similar layered compounds, such as $Na_3Ni_2SbO_6$[12] and Li_2MnO_3,[25,26] for which it was found that stacking defects along the monoclinic c axis caused this broadening. In a recent study concerning Li_2MnO_3, Boulineau et al. observed that the broadening decreases progressively with an increase in temperature.[26] The synthesis temperature influence on the $Li_3Ni_2BiO_6$ XRD pattern was then studied for various temperatures from 550 to 900 °C. With a long treatment at low temperature, the broadening is so significant that the diffraction peaks (020), (110), (−111), and (021) are convoluted in a unique asymmetric diffuse peak (see the Supporting Information, Figure S1a). A decrease of the broadening was noticed for synthesis temperatures higher than 700 °C; however, the final products are black and their XRD patterns show some impurities, especially $LiBiO_2$ and some lithium-doped nickel oxides (see the Supporting Information, Figure S1b).

Table 1 presents the cell parameters of $Li_3Ni_2BiO_6$ and compares them to those of similar honeycomb-ordered layered compounds. It is observed that the increase of the cell parameters a, b, and c is directly related to an increase of the ionic radii of M^{2+} and/or X^{5+}: i.e., the sum $r(M^{2+}) + r(X^{5+})$. As the Bi^{5+} ionic radius is larger than that of Sb^{5+},[27] $Li_3Ni_2BiO_6$ and $Li_3Zn_2BiO_6$ phases have larger cell parameters compared to those of phases containing the Sb^{5+} cation.

SEM analysis was carried out in order to visualize the grain size and morphology of $Li_3Ni_2BiO_6$. As shown in Figure 3, the particle distribution is relatively homogeneous with an average size of less than 1 μm. The layered character that can be usually seen in some lamellar AMO_2 compounds is not very significant here. However, the general flakelike grain shape is evident here.

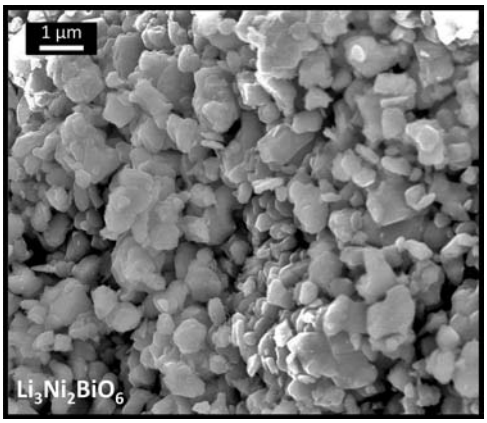

Figure 3. SEM picture of an $Li_3Ni_2BiO_6$ powder sample.

b. Stacking Fault Simulation in $Li_3Ni_2BiO_6$. The presence of the light elements lithium and oxygen as well as the stacking defects prevents a reliable structural characterization by the Rietveld technique from the XRD patterns. That explains why only profile-matching refinements are provided in this study. However, it seemed interesting to try to quantify the stacking defects by simulating their influence on an XRD pattern. This was performed with the DIFFaX program

Table 1. Cell Parameter Comparison between Different $Li_3M_2XO_6$ Layered Compounds[a]

composition	$r(M^{2+}) + r(X^{5+})$ (Å)	a (Å)	b (Å)	c (Å)	β (deg)	V (Å^3)
Li_2MnO_3[13]	1.29	4.937	8.532	5.030	109.46	199.8
$Li_3Ni_2SbO_6$[9]	1.29	5.1828	8.9677	5.1577	109.696	225.7
$Li_3Zn_2SbO_6$[6]	1.34	5.259	9.036	5.209	110.49	231.9
$Li_3Ni_2BiO_6$	1.49	5.2581(4)	9.116(1)	5.1969(8)	109.33(1)	235.1(9)
$Li_3Zn_2BiO_6$[6]	1.50	5.344	9.221	5.255	109.57	245.0

[a]The ionic radii sums $r(M^{2+}) + r(X^{5+})$ are calculated using data from Shannon et al.[27]

dx.doi.org/10.1021/ic300351t | Inorg. Chem. 2012, 51, 5377−5385

developed by Treacy and Newsam.[28] DIFFaX requires defining primary blocks of $Li_3Ni_2BiO_6$ that are then stacked following right or faulted vectors. Following previous works on Li_2MnO_3,[25,26] a unique type of block constituted by a slab and an interslab space has been considered. The experimental cell parameters of $Li_3Ni_2BiO_6$ are coupled with the atomic positions from $Li_3Zn_2SbO_6$.[6] Each block was then stacked over the previous one according to three possible vectors, (0; 0; 1), ($^1/_2$; $-^1/_6$; 1), and ($^1/_6$; $-^1/_6$; 1) in the monoclinic system. The exclusive occurrence of one of these vectors leads to a perfect stacking, while their alternation involves stacking defects. Figure 4a presents the simulated XRD patterns from an ideal to a completely disordered structure (i.e., from 0 to 100% of defects). A broadening of the all diffraction peaks (except the 00*l* ones) is clearly evident. In the same time the intensity of the (110), (−111), (021), and (111) peaks significantly decreases. The diffraction peak (110), which is more intense than the (020) peak for the ideal $Li_3Ni_2BiO_6$, becomes smaller for more than 5% of stacking defects (Figure 4b), which is in good agreement with what is experimentally observed in the inset of Figure 2. This simulation process enables us to estimate the stacking defects in $Li_3Ni_2BiO_6$ between 5 and 10%.

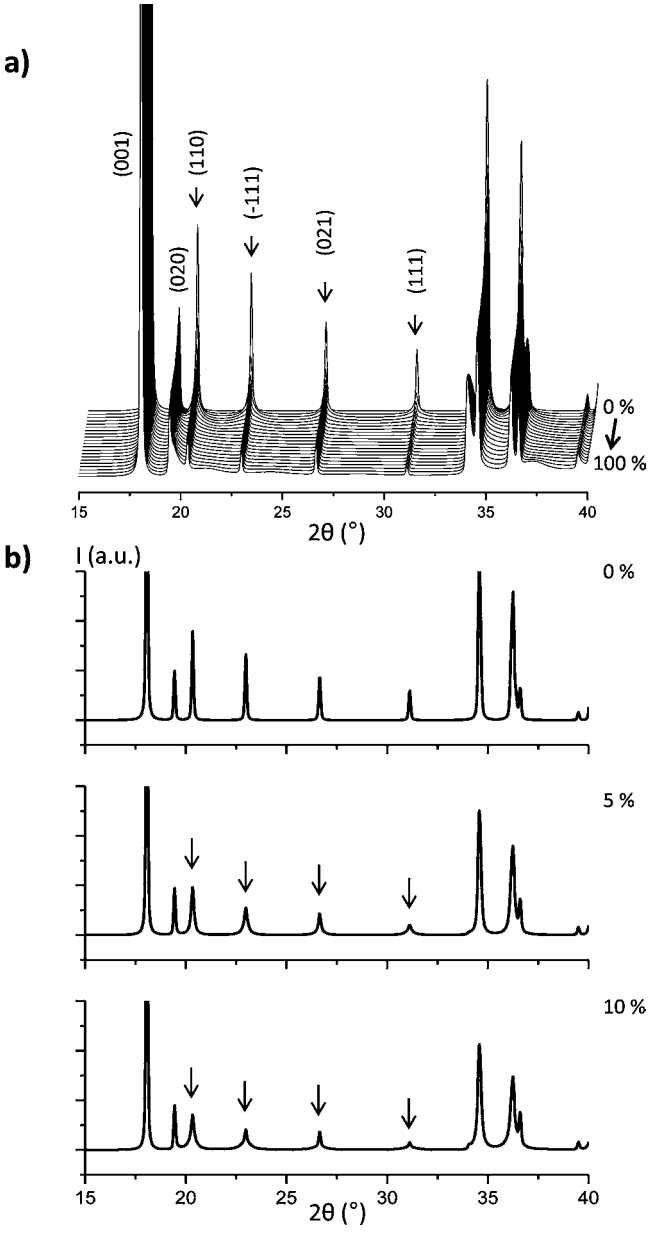

Figure 4. Simulated XRD patterns of $Li_3Ni_2BiO_6$ with stacking fault amounts from 0 to 100% (totally disordered) (a) and for respectively 0, 5, and 10% (b). A comparison with the experimental XRD pattern (inset of Figure 2) enables us to conclude that there are ∼5% of defects in $Li_3Ni_2BiO_6$.

c. Substituted $Li_3NiM'BiO_6$ Phases (with M′ = Mg, Cu, Zn). Ni^{2+} is not the only M^{2+} cation that can accommodate the octahedral site within the slabs in layered compounds. For example, with $Na_2M_2TeO_6$, M can be Mg, Mn, Co, Cu, or Zn.[10,20] During our study, we were unable to reproduce the work of Greaves et al. to obtain a pure $Li_3Zn_2BiO_6$ phase, and our attempts to form other $Li_3M_2BiO_6$ (with M = Mg, Mn, Co, Cu) phases were not successful. Other compositions with a partial substitution of the Ni^{2+} were then tried, especially the series $Li_3NiM'BiO_6$. The formation of single phases for the compositions $Li_3NiMgBiO_6$, $Li_3NiCuBiO_6$, and $Li_3NiZnBiO_6$ is clearly shown by XRD (Figure 5). No extra peaks that could be linked to an additional Ni^{2+}/M'^{2+} ordering within the honeycomb lattice are visible. The M'^{2+} cations are randomly located in the same site of the Ni^{2+} cations, and there is no intermixing with Bi^{5+} cations. The peak broadening observed for $Li_3Ni_2BiO_6$ at low 2θ angles is also present in the XRD patterns; therefore, a small amount of stacking faults can be assumed for all these $Li_3NiM'BiO_6$ phases. All powder samples are dark green. Table 2 presents the cell parameters of these three phases, obtained by profile-matching refinements using the same $C2/m$ space group. As was observed in Table 1, the cell parameter evolution is related to the ionic radii of M^{2+},

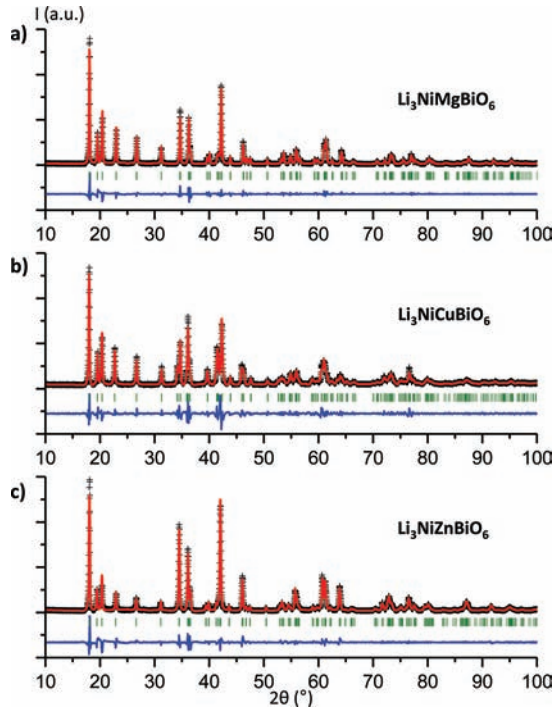

Figure 5. Experimental XRD patterns of (a) $Li_3NiMgBiO_6$, (b) $Li_3NiCuBiO_6$, and (c) $Li_3NiZnBiO_6$. Observed, calculated (profile matching), and difference profiles are given respectively by black crosses and red and blue lines. Bragg positions are given by green vertical lines.

dx.doi.org/10.1021/ic300351t | Inorg. Chem. 2012, 51, 5377−5385

Table 2. Cell Parameters of Different $Li_3NiM'BiO_6$ Phases (Space Group $C2/m$) and Comparison with $Li_3Ni_2BiO_6$ and $Li_3Zn_2BiO_6$[a]

composition	$r(Ni^{2+}) + r(M'^{2+})$ (Å)	a (Å)	b (Å)	c (Å)	β (deg)	V (Å^3)
$Li_3Ni_2BiO_6$	1.38	5.2581(4)	9.116(1)	5.1969(8)	109.33(1)	235.1(9)
$Li_3NiMgBiO_6$	1.41	5.2612(7)	9.097(1)	5.2212(6)	109.62(1)	235.4(9)
$Li_3NiCuBiO_6$	1.42	5.314(1)	9.087(2)	5.269(1)	110.55(1)	238.2(9)
$Li_3NiZnBiO_6$	1.43	5.2831(8)	9.150(1)	5.226(1)	109.61(1)	237.9(9)
$Li_3Zn_2BiO_6$[6]	1.48	5.344	9.221	5.255	109.57	245.0

[a]The ionic radii sums $r(Ni^{2+}) + r(M'^{2+})$ are calculated using data from Shannon et al.[27] The cell parameter evolution follows a regular trend according to the different ionic radii, except for $Li_3NiCuBiO_6$.

M'^{2+}, and Bi^{5+}. Therefore, for $Li_3NiM'BiO_6$ phases, the substitution of half the Ni^{2+} cations by slightly larger cations, such as Mg^{2+}, Cu^{2+}, and Zn^{2+},[27] translates to greater unit cell parameters. This general cell parameter trend is, however, not fully respected for $Li_3NiCuBiO_6$, which is indeed characterized by larger a and c and smaller b parameters and a significantly different β angle. This result may be related to an active Jahn–Teller effect of the Cu^{2+} involving local CuO_6 octahedral distortion.

d. Magnetic Properties. In the $Li_3Ni_2BiO_6$ and $Li_3NiM'BiO_6$ (with M′ = Mg, Zn) phases, only the Ni^{2+} cations ($3d^8$, $S = 1$) contribute to the magnetic behavior, whereas in $Li_3NiCuBiO_6$, Cu^{2+} cations ($3d^9$, $S = {}^1/_2$) also contribute. The temperature-dependent magnetic susceptibility data for a polycrystalline sample of $Li_3Ni_2BiO_6$ are shown in Figure 6.

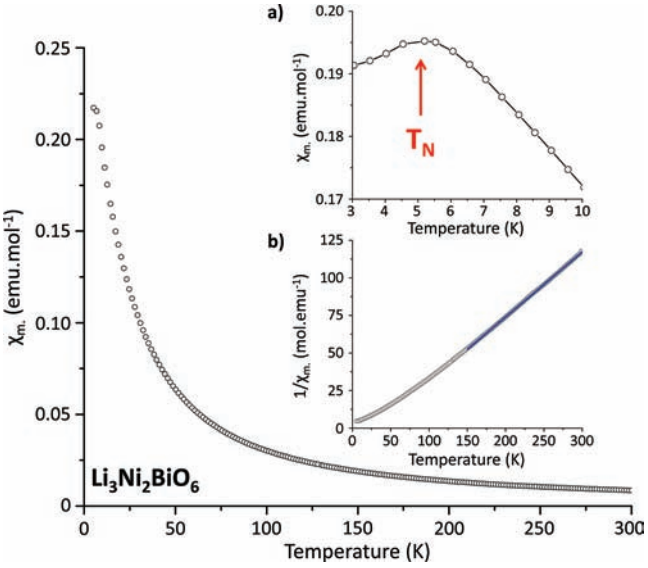

Figure 6. Magnetic susceptibility evolution in the temperature range 5–300 K for $Li_3Ni_2BiO_6$. The low-temperature AFM ordering is evidenced in the inset (a). The linear evolution of the inverse susceptibility can be fitted using a Curie–Weiss law (inset (b), blue solid lines).

It exhibits a general paramagnetic behavior, and the inverse of the magnetic susceptibility follows a linear trend that has been fitted between 150 and 300 K with the Curie–Weiss law $\chi = C/(T - \Theta)$. The effective magnetic moment μ_{eff} is 4.34 μ_B (i.e., 3.07 μ_B/Ni^{2+}), which is in good agreement with the theoretical value, assuming the magnetism results from Ni^{2+} cations with spin-only contributions (μ_{theor} = 4.00 μ_B, i.e. 2.83 μ_B/Ni^{2+}). The Weiss constant is positive (27 K), indicating ferromagnetic short-range interactions.

The slightly higher experimental value of the effective moment can be explained by the spin–orbital coupling, which will often increase the observed moment in the case of elements with more than half-filled d orbitals.[29−32] In their recent study on the similar honeycomb-ordered layered $Li_3Ni_2SbO_6$ phase, Zvereva et al. observed an effective moment of 4.3 μ_B and found a significantly positive Weiss constant (8 K),[9] which is in good agreement with the results obtained on $Li_3Ni_2BiO_6$. However, the authors used in their study an additional temperature-independent term χ_0 in their Curie–Weiss law fitting: $\chi = C/(T - \Theta) + \chi_0$. For $Li_3Ni_2SbO_6$, the weak positive value of χ_0 was attributed to the predominance of Ni^{2+} Van Vleck paramagnetic contributions over diamagnetic contributions. Therefore, magnetic data of $Li_3Ni_2BiO_6$ were fitted a second time, taking into account this additional term. The resulting negative value of χ_0 slightly increases the total effective moment to 4.52 μ_B (Table 3) and demonstrates that Ni^{2+} Van Vleck paramagnetic contributions may not be as predominant as they are in $Li_3Ni_2SbO_6$. In addition, it is interesting to note that the total effective moment now matches well with that expected by using a Ni^{2+} moment of 3.2 μ_B, as is commonly observed in the literature.[30,33,34] At very low temperature, an antiferromagnetic ordering is present, with a maximum of the magnetic susceptibility (Néel temperature) around 5.5 K (Figure 6, inset a). This transition was also noticed in $Li_3Ni_2SbO_6$ at a slightly higher temperature (15 K).[9]

The temperature-dependent magnetic susceptibility data for polycrystalline samples of $Li_3NiM'BiO_6$ (M′ = Mg, Cu, Zn) are shown in Figure 7. They all exhibit a paramagnetic behavior over the whole temperature range. As for $Li_3Ni_2BiO_6$, magnetic data were fitted following a Curie–Weiss law, and the results are gathered in Table 3. For $Li_3NiMgBiO_6$ and $Li_3NiZnBiO_6$, elimination of half the nickel by nonmagnetic cations obviously decreases the total effective magnetic moment (2.84 and 2.90 μ_B, respectively). The values are closer to the spin-only theoretical values as the spin–orbital coupling decreases with a lower amount of Ni^{2+}. In $Li_3NiCuBiO_6$, the experimental total effective moment value of 3.38 μ_B agrees with the assumption of Ni^{2+} and Cu^{2+} cations with spin-only contributions (μ_{theor} = 3.32 μ_B). The second Curie–Weiss fitting with the additional term χ_0 does not significantly modify the calculated values of the effective moments. The only noticeable change is the Weiss constant observed for $Li_3NiCuBiO_6$, which shifts to 11 K. This positive value is more consistent with those obtained for $Li_3NiMgBiO_6$ and $Li_3NiZnBiO_6$. It is interesting to note that no antiferromagnetic ordering was evidenced at very low temperature for all $Li_3NiM'BiO_6$ phases, which suggests that the antiferromagnetic ground state stems from Ni^{2+}–O–Ni^{2+} interactions.

e. Electrochemical Properties of $Li_3Ni_2BiO_6$. The layered structure with the presence in the slabs of Ni^{2+} cations that can

dx.doi.org/10.1021/ic300351t | Inorg. Chem. 2012, 51, 5377–5385

Table 3. Magnetic Data Obtained for $Li_3Ni_2BiO_6$ and $Li_3NiM'BiO_6$ Phases from the Curie–Weiss Law Fitting from 150 to 300 K, with or without the Temperature-Independent Term χ_0

	$Li_3Ni_2BiO_6$	$Li_3NiMgBiO_6$	$Li_3NiCuBiO_6$	$Li_3NiZnBiO_6$
Theoretical Moment				
μ_{theor} based on spin-only contributions (μ_B)	4.00	2.83	3.32	2.83
μ_{theor} based on reported experimental moments for Ni^{2+} (3.2 μ_B) and Cu^{2+} (1.9 μ_B)[30,33,34]	4.52	3.2	3.72	3.2
Curie–Weiss Fitting				
Curie constant C (emu mol^{-1})	2.334(3)	1.005(1)	1.419(2)	1.042(1)
Weiss constant Θ (K)	27.1(2)	37.4(2)	−0.7(2)	33.2(2)
fitting factor R^2 (%)	99.989	99.987	99.986	99.987
effective moment μ_{eff} (μ_B)	4.34	2.84	3.38	2.90
Curie–Weiss with χ_0 Fitting				
Curie constant C (emu.mol^{-1})	2.53(2)	1.06(1)	1.256(3)	0.962(6)
Weiss constant Θ (K)	20.1(6)	33.3(8)	11.3(2)	39.6(5)
χ_0 (10^{-4} emu mol^{-1})	−5.3(4)	−1.5(3)	3.99(9)	2.3(2)
fitting factor R^2 (%)	99.9996	99.99	99.999	99.9995
effective moment μ_{eff} (μ_B)	4.52	2.92	3.18	2.79

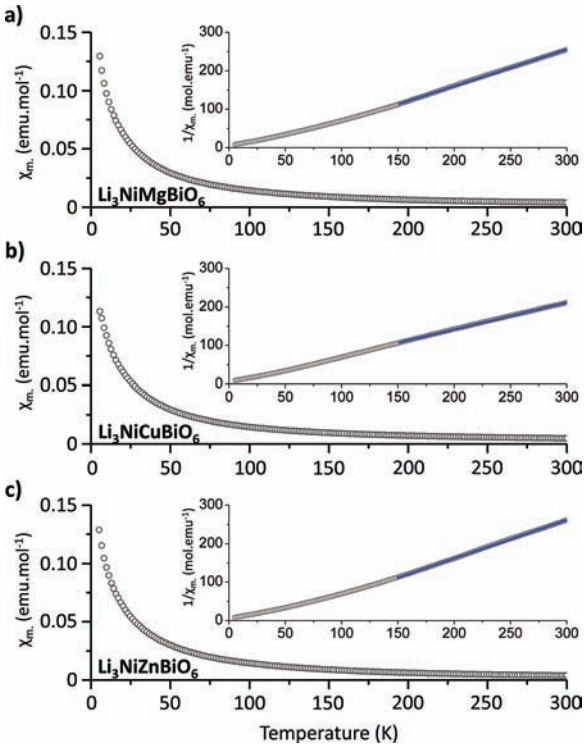

Figure 7. Magnetic susceptibility evolution in the temperature range 5–300 K for (a) $Li_3NiMgBiO_6$, (b) $Li_3NiCuBiO_6$, and (c) $Li_3NiZnBiO_6$. In the insets, the linear evolution of the inverse susceptibility can be fitted using a Curie–Weiss law (blue solid lines).

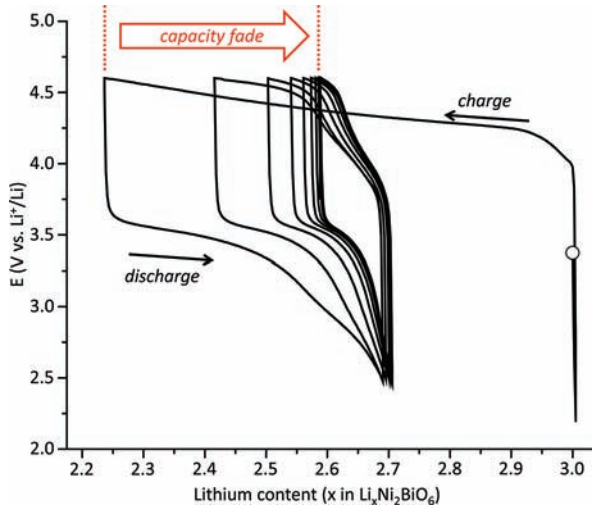

Figure 8. Electrochemical behavior of $Li_3Ni_2BiO_6$ as the positive electrode material of a lithium battery. The starting point is marked by the empty circle. The charge and discharge rate is C/20.

be oxidized during lithium extraction allows an investigation of the electrochemical properties of $Li_3Ni_2BiO_6$. However, because of its high molar mass, the study represents more a fundamental interest. Figure 8 shows the first electrochemical cycling obtained in a galvanostatic mode with $Li_3Ni_2BiO_6$ as the positive electrode of a lithium battery. The initial potential of 3.37 V vs Li^+/Li dramatically drops by starting the cycling in discharge. Therefore, it appears impossible to intercalate lithium ions in the initial material, which confirms the $Li_3Ni_2BiO_6$ composition as totally filled interslabs. The electrochemical curve does not present any plateau during the cycling, showing that the material remains a single phase. Only 0.75 lithium ion can be extracted during the first charge up to 4.6 V vs Li^+/Li, while 0.45 can be intercalated in the first discharge. The first discharge capacity is 81.7 mAh g^{-1}, which is significantly lower than a theoretical value of 181.5 mAh g^{-1} but very close to what was obtained for the similar honeycomb-ordered layered phase $Li_3Ni_2SbO_6$ (92 mAh g^{-1}).[8] After this first charge/discharge cycling, the capacity still decreases to 22 mAh g^{-1} after 10 cycles.

The electrochemical deintercalation and intercalation of lithium ions are possible; however, the capacity is very limited. In their study of the electrochemical properties of $Li_3Ni_2SbO_6$, Ma et al. reported that the Li/Ni interlayer mixing—originally negligible—dramatically increases up to 10% during the galvanostatic cycling.[8] The authors investigated the nickel migration into lithium vacancies and found a relatively low migration barrier which makes possible this Li/Ni mixing and leads to a rapid capacity fade. Therefore, the capacity decrease observed for $Li_3Ni_2BiO_6$ can be explained by a similar Li/Ni interlayer mixing.

f. $Ag_3Ni_2BiO_6$ Obtained by Topotactic Ionic Exchange. New structures obtained by topotactic ionic exchanges are known to be very influenced by the stacking nature of the precursor, especially the crystallographic site accommodated by A^+ cations. For example, three different $AgCoO_2$ polytypes can

dx.doi.org/10.1021/ic300351t | Inorg. Chem. 2012, 51, 5377–5385

be obtained by ion exchange using O3-$LiCoO_2$, P2−Na_xCoO_2, or the mixed layered phase OP4-$Li_xNa_yCoO_2$.[5] In the case of delafossite $AgNiO_2$, topotactic exchanges from $ANiO_2$ precursors (A = Li, Na, K with an O3 stacking) lead to the rhombohedral polytype.[35−37] The hexagonal polytype can be alternatively prepared by a coprecipitation method.[38]

The topotactic process can affect the slab positions, but any possible cation ordering within the slabs remains the same. This has been verified by Politaev et al. when they reported the synthesis of honeycomb-ordered $Ag_3Co_2SbO_6$ delafossite from the layered precursor $Na_3Co_2SbO_6$.[12] Indeed, an enlarged cell (compare to the hexagonal for $AgCoO_2$) was necessary to take into account the superstructure peaks related to the Co^{2+}/Sb^{5+} ordering.

In the present study the molten salt ion exchange was performed using $Li_3Ni_2BiO_6$ as the layered precursor. The final product obtained after washing and drying is black. The corresponding XRD powder pattern is shown in Figure 9. It can

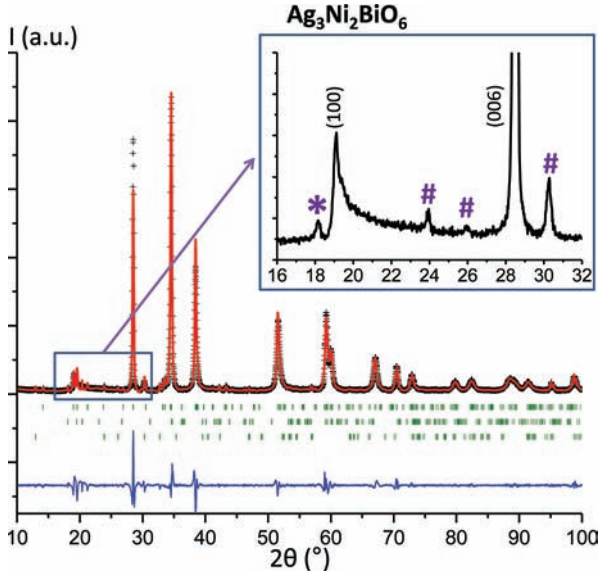

Figure 9. Experimental XRD pattern of $Ag_3Ni_2BiO_6$ (observed, calculated (profile matching), and difference profiles given respectively as black crosses and red and blue lines; Bragg positions as green vertical lines). The inset highlights the peak broadening, on the right side of the (100) peak (dashed blue line), explained by stacking faults. Impurities are marked by the following symbols: * for remaining $Li_3Ni_2BiO_6$ and # for bismutite $Bi_2O_2(CO_3)$.

be indexed using the space group $P3_112$, the same as for $Ag_3Co_2SbO_6$. The cell parameters, obtained by profile-matching refinement, are a = 5.4012(8) Å and c = 18.795(4) Å. In comparison with $AgNiO_2$ delafossite (a = 5.090 Å and c = 18.37 Å, experimental values from Shin et al.[37] are adapted in an enlarged cell), the larger a and c parameters are explained by the larger ionic radii, especially Bi^{5+}, but also Ni^{2+} in comparison to Ni^{3+}.[27] However, some weak impurity diffraction peaks of bismutite $Bi_2O_2(CO_3)$ are noticed in the XRD pattern (inset of Figure 9). Also, a very small amount of the precursor $Li_3Ni_2BiO_6$ is still present. This result was expected, as it is always very difficult to totally exchange Li^+ in the octahedral site by Ag^+ in a dumbbell configuration.[39] Preliminary ball milling of the $Li_3Ni_2BiO_6$ powder in order to reduce the grain size or repetition of the exchange treatment slightly improved the exchange yield, but it finally appeared impossible to exchange all of the precursor. ICP analysis shows a cationic ratio Li/(Ni + Bi) lower than 0.1. Therefore, more than 90% of the lithium ions have been exchanged during the molten salt treatment, which is a very acceptable yield.

$Ag_3Ni_2BiO_6$ is, to the best of our knowledge, the first reported delafossite which contains a Bi^{5+} cation. Its structure is shown in Figure 10. As the stacking nature of $Li_3Ni_2BiO_6$ is O3

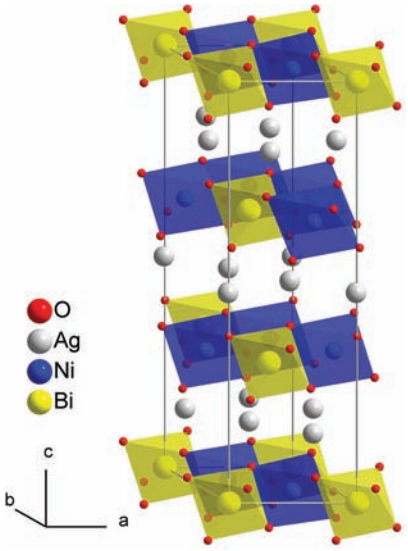

Figure 10. Representation in a perspective view of the $Ag_3Ni_2BiO_6$ delafossite structure. The honeycomb Ni^{2+}/Bi^{5+} ordering is evidenced within the $Ni_{2/3}Bi_{1/3}O_2$ slabs (blue and yellow edge-shared octahedra), while Ag cations (in gray) occupy dumbbell linear sites.

(O3*S* regarding the honeycomb ordering), $Ag_3Ni_2BiO_6$ structure is the D3 delafossite polytype (or D3*S*). A slab-gliding process is necessary during the topotactic ionic exchange in order to create the linear dumbbell site that silver cations can accommodate.[5] The diffuse and asymmetric peak—also present in the case of $Ag_3Co_2SbO_6$[12]—is obviously related to stacking defects. It seems to be more visible than in $Li_3Ni_2BiO_6$, as supplementary faults may occur during the ionic exchange and are added to the initial stacking faults of the precursor. These stacking faults prevent deeper structural characterization.

Compounds obtained by ionic exchange are known to have a relatively weak thermal stability. TGA was then performed on $Ag_3Ni_2BiO_6$ to determine its stability and to compare it with that of similar compounds. Figure 11 shows the mass evolution until 800 °C. The unique and significant mass loss just above 400 °C stands for the decomposition of the delafossite compound. This value is very close to the decomposition temperature of $AgNiO_2$.[36] The post-TGA products were determined by XRD to be nickel and bismuth oxides as well as silver metal. Therefore, the mass loss is attributed to oxygen departure according to eq 2, and its experimental value of 5.4%

$$Ag_3Ni_2BiO_6 \rightarrow {}^1/_2Bi_2O_3 + 2NiO + 3Ag + {}^5/_4O_2 \qquad (2)$$

perfectly matches with a theoretical loss of 5.36%. As there is only one mass loss, the reductions of silver and bismuth occur in the same temperature range. Note that this TGA analysis neglected the minor aforementioned impurities present in the final product.

dx.doi.org/10.1021/ic300351t | Inorg. Chem. 2012, 51, 5377−5385

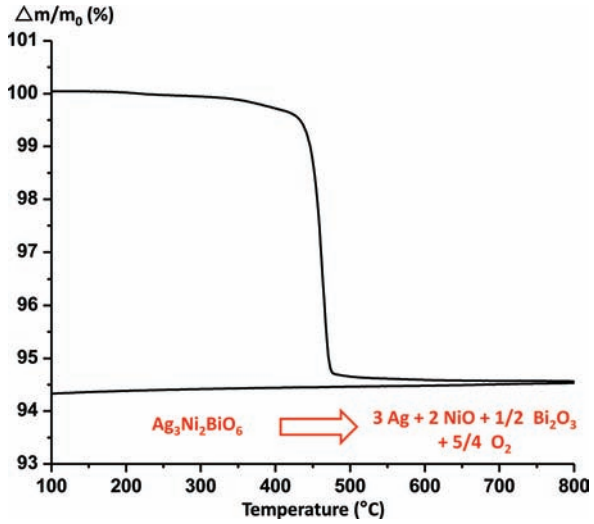

Figure 11. Thermogravimetric analysis evidencing the weak stability of the delafossite $Ag_3Ni_2BiO_6$ formed by ionic exchange.

CONCLUSION

The new layered compound $Li_3Ni_2BiO_6$ was prepared by a conventional solid-state reaction. Its lamellar structure is analogous to that of several other $A_3M_2XO_6$ compounds and is characterized by a honeycomb ordering between Ni^{2+} and Bi^{5+} cations within the slabs. $Li_3Ni_2BiO_6$ crystallizes in a monoclinic cell (space group $C2/m$) with the parameters a = 5.2581(4) Å, b = 9.116(1) Å, c = 5.1969(8) Å, and β = 109.33(1)°. However, some stacking faults are present and weakly alter some specific diffraction peaks. A DIFFaX simulation enables us to estimate a stacking defect concentration of approximately 5%. $Li_3Ni_2BiO_6$ presents a paramagnetic behavior at high temperature and an antiferromagnetic transition at 5.5 K. As for the $Li_3Ni_2SbO_6$ analogue, the electrochemical deintercalation and intercalation of lithium ions is possible; however, the battery capacity is rather limited, certainly due to Li/Ni mixing occurring during the electrochemical cycling.

Three other phases have been successfully prepared by substituting half of the Ni^{2+} cations by Mg^{2+}, Cu^{2+}, and Zn^{2+}. They are isostructural with $Li_3Ni_2BiO_6$ and present a paramagnetic behavior with, however, no evidence of antiferromagnetic transitions down to 3 K.

By topotactic molten salt ionic exchange, the new delafossite phase $Ag_3Ni_2BiO_6$ was obtained from $Li_3Ni_2BiO_6$. It crystallizes in hexagonal symmetry with the cell parameters a = 5.4012(8) Å and c = 18.795(4) Å, and it is still characterized by the Ni^{2+}/Bi^{5+} honeycomb ordering. As for other delafossites obtained by ionic exchange, $Ag_3Ni_2BiO_6$ has limited thermal stability, as it decomposes above 400 °C.

ASSOCIATED CONTENT

Supporting Information

Figures giving experimental XRD patterns of $Li_3Ni_2BiO_6$ obtained at 550 and at 900 °C. This material is available free of charge via the Internet at http://pubs.acs.org.

AUTHOR INFORMATION

Corresponding Author

*E-mail: mas.subramanian@oregonstate.edu.

Notes

The authors declare no competing financial interest.

ACKNOWLEDGMENTS

This work has been supported by NSF Grant DMR 0804167. We thank Mike Treacy (Arizona State University) and Laurence Croguennec (ICMCB-CNRS) for useful discussions concerning DIFFaX simulations and both Dany Carlier and Marie Guignard (ICMCB-CNRS) for technical assistance with and fruitful discussions on the electrochemical study.

REFERENCES

(1) Mizushima, K.; Jones, P.; Wiseman, P.; Goodenough, J. *Mater. Res. Bull.* **1980**, *15*, 783−789.
(2) Kawazoe, H.; Yasukawa, M.; Hyodo, H.; Kurita, M.; Yanagi, H.; Hosono, H. *Nature* **1997**, *389*, 939−942.
(3) Shannon, R. D.; Rogers, D. B.; Prewitt, C. T. *Inorg. Chem.* **1971**, *10*, 713−718.
(4) Delmas, C.; Fouassier, C.; Hagenmuller, P. *Physica B+C* **1980**, *99*, 81−85.
(5) Berthelot, R.; Pollet, M.; Doumerc, J.-P.; Delmas, C. *Inorg. Chem.* **2011**, *50*, 4529−4536.
(6) Greaves, C.; Katib, S. *Mater. Res. Bull.* **1990**, *25*, 1175−1182.
(7) Skakle, J.; Castellanos, R.; M., Tovar, S.; West, A. *J. Solid State Chem.* **1997**, *131*, 115−120.
(8) Ma, X.; Kang, K.; Ceder, G.; Meng, Y. S. *J. Power Sources* **2007**, *173*, 550−555.
(9) Zvereva, E. A.; Evstigneeva, M. A.; Nalbandyan, V. B.; Savelieva, O. A.; Ibragimov, S. A.; Volkova, O. S.; Medvedeva, L. I.; Vasiliev, A. N.; Klingeler, R.; Buechner, B. *Dalton Trans.* **2012**, *41*, 572−580.
(10) Viciu, L.; Huang, Q.; Morosan, E.; Zandbergen, H.; Greenbaum, N.; McQueen, T.; Cava, R. J. *J. Solid State Chem.* **2007**, *180*, 1060−1067.
(11) Smirnova, O.; Nalbandyan, V.; Petrenko, A.; Avdeev, M. *J. Solid State Chem.* **2005**, *178*, 1165−1170.
(12) Politaev, V.; Nalbandyan, V.; Petrenko, A.; Shukaev, I.; Volotchaev, V.; Medvedev, B. *J. Solid State Chem.* **2010**, *183*, 684−691.
(13) Strobel, P.; Lambert-Andron, B. *J. Solid State Chem.* **1988**, *75*, 90−98.
(14) James, A.; Goodenough, J. *J. Solid State Chem.* **1988**, *74*, 287−294.
(15) O'Malley, M. J.; Verweij, H.; Woodward, P. M. *J. Solid State Chem.* **2008**, *181*, 1803−1809.
(16) Kataoka, K.; Takahashi, Y.; Kijima, N.; Nagai, H.; Akimoto, J.; Idemoto, Y.; Ohshima, K.-I. *Mater. Res. Bull.* **2009**, *44*, 168−172.
(17) Betz, T.; Hoppe, R. *Z. Anorg. Allg. Chem.* **1984**, *512*, 19−33.
(18) Morss, L.; Appelman, E.; Gerz, R.; Martin-Rovet, D. *J. Alloys Compd.* **1994**, *203*, 289−295.
(19) Xu, J.; Assoud, A.; Soheilnia, N.; Derakhshan, S.; Cuthbert, H. L.; Greedan, J. E.; Whangbo, M. H.; Kleinke, H. *Inorg. Chem.* **2005**, *44*, 5042−5046.
(20) Evstigneeva, M. A.; Nalbandyan, V. B.; Petrenko, A. A.; Medvedev, B. S.; Kataev, A. A. *Chem. Mater.* **2011**, *23*, 1174−1181.
(21) Nagarajan, R.; Uma, S.; Jayaraj, M.; Tate, J.; Sleight, A. *Solid State Sci.* **2002**, *4*, 787−792.
(22) Climent-Pascual, E.; Norby, P.; Andersen, N.; Stephens, P.; Zandbergen, H.; Larsen, J; Cava, R. J. *Inorg. Chem.* **2012**, *51*, 557−565.
(23) Hosogi, Y.; Kato, H.; Kudo, A. *J. Mater. Chem.* **2008**, *18*, 647−653.
(24) Todorova, V.; Leineweber, A.; Kienle, L.; Duppel, V.; Jansen, M. *J. Solid State Chem.* **2011**, *184*, 1112−1119.
(25) Bréger, J.; Jiang, M.; Dupré, N.; Meng, Y. S.; Shao-Horn, Y.; Ceder, G.; Grey, C. P. *J. Solid State Chem.* **2005**, *178*, 2575−2585.
(26) Boulineau, A.; Croguennec, L.; Delmas, C.; Weill, F. *Solid State Ionics* **2010**, *180*, 1652−1659.
(27) Shannon, R. D. *Acta Crystallogr. Sect. A* **1976**, *32*, 751−767.
(28) Treacy, M.; Newsam, J.; Deem, M. *Proc. R. Society London, Ser. A* **1991**, *433*, 499−520.

(29) Goodenough, J. B. *Magnetism and the Chemical Bond*; Robert E. Krieger Publishing: Huntington, NY, 1976.
(30) Ashcroft, N. W.; Mermin, N. D. *Solid State Physics*; Brooks/Cole: Belmont, CA, 1976.
(31) Cox, P. A. *The Electronic Structure and Chemistry of Solids*; Oxford Science Publications: Oxford, U.K., 1987.
(32) Kittel, C. *Introduction to Solid State Physics*, 8th ed.; Wiley: Hoboken, NJ, 2005.
(33) Van Vleck, J. H. *The Theory of Electric and Magnetic Susceptibilities*; Oxford University Press: Oxford, U.K., 1952.
(34) Kubo, R., Nagamiya, T. *Solid State Physics*; McGraw-Hill: New York, 1969.
(35) Bityutskii, P. N.; Khitrova, V. I. *J. Struct. Chem.* **1969**, *9*, 921−925.
(36) Wichainchai, A.; Dordor, P.; Doumerc, J.-P.; Marquestaut, E.; Pouchard, M.; Hagenmuller, P. *J. Solid State Chem.* **1988**, *74*, 126−131.
(37) Shin, Y.; Doumerc, J.-P.; Dordor, P.; Delmas, C.; Pouchard, M.; Hagenmuller, P. *J. Solid State Chem.* **1993**, *107*, 303−313.
(38) Sörgel, T.; Jansen, M. *Z. Anorg. Allg. Chem.* **2005**, *631*, 2970−2972.
(39) Berthelot, R.; Pollet, M.; Doumerc, J.-P.; Delmas, C. *Inorg. Chem.* **2011**, *50*, 6649−6655.

dx.doi.org/10.1021/ic300351t | *Inorg. Chem.* 2012, 51, 5377−5385